nature geoscience

LETTERS

PUBLISHED ONLINE: 13 FEBRUARY 2011 | DOI: 10.1038/NGEO1080

Dominant role of tectonic inheritance in supercontinent cycles

Pascal Audet* and Roland Bürgmann

Supercontinents episodically assemble and break up, in association with the closure and opening of ocean basins[1]. During these cycles, continental margins are repeatedly weakened and deformed during subduction, orogeny and rifting, whereas continental cores tend to remain intact[2,3]. It has therefore been suggested that deformation during supercontinent cycles is controlled by the pre-existing structure of the lithosphere, for example by rheological heterogeneities and mechanical anisotropy that were acquired during past tectonic events[4,5]. However, observational constraints for this idea have been lacking. Here we present global, high-resolution maps of the lithosphere's effective elastic thickness over the continents—a proxy for the rigidity or long-term strength of the lithosphere—calculated from a comparison of the spectral coherence between topography and gravity anomalies and the flexural response of an equivalent elastic plate to loading. We find that effective elastic thickness is high in Archean cratons, but low in the surrounding Phanerozoic belts. We also estimate the anisotropy in effective elastic thickness, indicative of a directional dependence of lithospheric rigidity, and show that directions of mechanical weakness align with large gradients in effective elastic thickness and with tectonic boundaries. Our findings support the notion that lithospheric rigidity is controlled by pre-existing structure, and that during the supercontinent cycle, strain is concentrated at pre-existing zones of weakness.

The Earth has experienced several supercontinent cycles since 2.7 Gyr, the last one ending with the breakup of Pangaea into the current plate configuration. The driving mechanism is associated with vertical motion of the convective mantle from both subduction of ocean basins during supercontinent assembly and warm mantle upwelling causing breakup and the creation of new ocean floor[6]. Although the details of the dynamics are still debated[7–9], it is generally agreed that continental margins are repeatedly deformed within weak, diffuse zones, and that stronger cratonic lithosphere remains intact during this process[2]. Most cratonic cores within continents show crustal ages greater than 2.0 Gyr, are depleted in basaltic constituents and conductively cooled through time, thus acquiring a thick, high-viscosity thermo-chemical root[2]. Continental margins, in contrast, are much younger (<0.5 Gyr), have been thermally rejuvenated and structurally reactivated[4], and are much thinner. Such large differences in structure imply comparably large gradients in rheological properties of the lithosphere. These factors, combined with numerical simulations of coupled mantle convection and continental plates, indicate that deformation during supercontinent cycles may be controlled by pre-existing structure acquired from past tectonic events[4,5]. There is little observational constraint, however, on the spatial variability of rheological properties of the lithosphere because it cannot be observed directly[10].

A useful proxy for the long-term strength of the lithosphere is given by the flexural rigidity, $D = ET_e^3/12(1-\nu^2)$, where E is Young's modulus and ν is Poisson's ratio, which governs the resistance to vertical flexure[10]. The strong dependence of D on T_e implies that the magnitude and spatial variations of T_e can have a significant influence on the degree and style of deformation as a result of long-term tectonic loads[11]. In particular, it is expected that spatial variations and gradients in T_e can prescribe where strain may localize and consequently determine the locus of deformation as manifested by brittle (for example seismicity, faulting) and thermal processes (for example volcanism, rifting). T_e is estimated by comparing the spectral coherence between topography and Bouguer gravity anomalies with that predicted for an equivalent elastic plate bending under surface and internal loading[10]. The plate response is modelled either as isotropic or anisotropic, and the coherence is inverted for a single parameter, T_e, or the three parameters of an orthotropic elastic plate (that is, having different rigidities in two perpendicular directions), T_{min}, T_{max}, and ϕ_e, the direction of weakest rigidity[12]. Here we use the wavelet transform method to calculate the coherence and estimate T_e and T_e anisotropy[12,13] and apply the technique to all major continents, with the exception of Greenland and Antarctica where thick ice caps complicate the analysis and data coverage is incomplete. We account for possible bias in T_e estimation by considering the effect of gravitational 'noise' (as defined by refs 14,15) and masking regions where the model fails[15]. Regions where bias is strongest generally coincide with areas where topography is low[14,15] (Fig. 1a), although the converse is not true in general. A discussion of the technique, error analysis and 'noise' bias is included in the Supplementary Information.

Figure 1a shows the azimuthal variations of the weak direction of T_e superposed on the pattern of T_e variations. The results are in agreement with a global, low-resolution compilation of T_e from various sources and techniques[10], and with regional studies that use high-resolution gravity-topography coherence mapping[12,13,15–19]. In general the T_e pattern correlates with age since the last thermo-tectonic event[20], consistent with previous regional findings[15–19]. T_e is high (>100 km) in Early to Late Proterozoic and Archean cratonic provinces, with the largest values found in the North American, West African, and East European shields. Some cratons (for example South Africa, North China, South India) exhibit lower T_e ($50 < T_e < 100$ km), where lithosphere has been thinned by plume-related magmatism or delamination. Low T_e (<40 km) is found in young Phanerozoic orogens (for example American Cordillera, Alpide belt) and tectonically active provinces (for example western North America, Afar Triple Junction and most of central-eastern Asia). T_e is also generally low in the hanging wall of past and present subduction zones and along most continental margins, possibly the result of thermal and fluid-related weakening as a consequence of subduction and rifting processes[10,21].

Berkeley Seismological Laboratory and Department of Earth and Planetary Science, Berkeley, California 94720, USA. *e-mail: paudet@berkeley.edu.

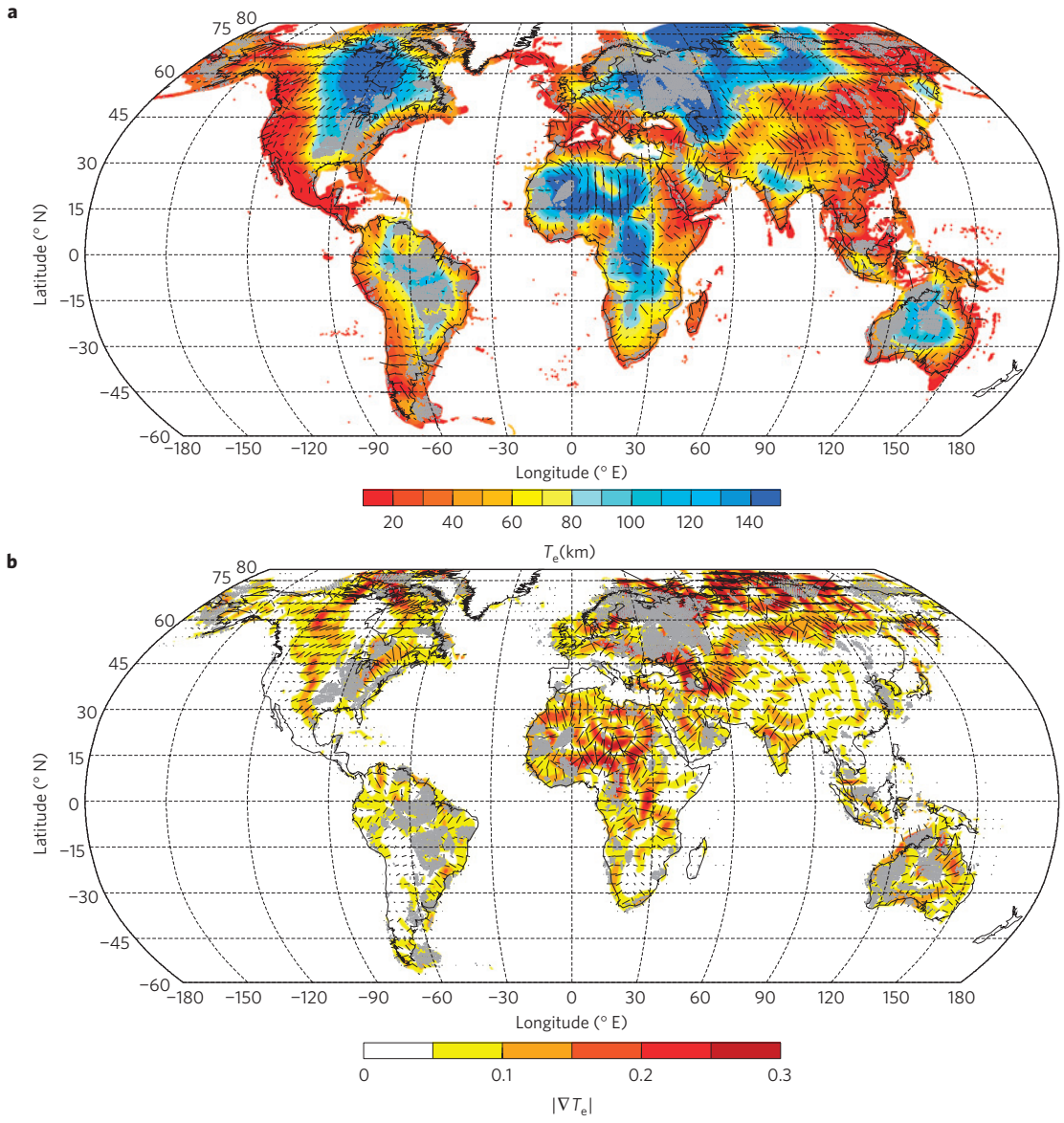

Figure 1 | Global effective elastic thickness over continents calculated from the coherence between Bouguer gravity and topography using a wavelet transform. a, T_e anisotropy (sampled on a 3° × 3° grid) superposed on filtered (using a Gaussian function of width 900 km) and colour-contoured T_e over continents and continental shelves (depth shallower than 500 m below sea level). Shaded areas correspond to regions where T_e estimation is biased by gravitational 'noise'[14,15]. The length of black bars is given by the magnitude of T_e anisotropy from the ratio $(T_{max} - T_{min})/(T_{max} + T_{min})$. **b**, Magnitude and direction of T_e gradient. All images are in a Robinson projection with a central meridian of 0° longitude.

To examine the factors controlling T_e variations, we compare the T_e map with global surface heat flux[20] (q_s) and global seismic velocity anomalies ($\delta v_s/v_s$) at 100 km depth[22,23] (Fig. 2a,b). We find a good correlation ($r > 0.64$) with both published seismic models, indicating that seismic velocities and T_e are sensitive to the same range of parameters, mainly temperature and composition (and thus geotherm[24]). However, we do not find a statistically significant relationship between T_e and heat flow ($r = -0.32$). One reason for this discrepancy is the effect produced by significant upper-crustal heat generation on surface heat flow. As such, q_s is a poor indicator of lithosphere geotherm and does not provide a good measure of lithosphere mantle temperature, and thus temperature-dependent creep strength, on continents. Finally, we find a good correlation between low T_e and active tectonic processes: more than 70% of seismicity (for events shallower than 50 km) and volcanic centres concentrate where $T_e < 40$ km (Fig. 2c,d).

T_e anisotropy varies over short spatial scales (~200–500 km) in both magnitude and direction (Fig. 1a), thus ruling out a deep, sub-lithospheric mantle-flow origin. Magnitude of T_e anisotropy is inversely correlated with T_e, as young, low-T_e provinces exhibit larger magnitude than older, high-T_e cratons. T_e anisotropy reflects directional variations in the flexural compensation of the lithosphere and has been speculated to originate from two competing effects: dynamical[17,25] (for example in-plane stress-weakening and basal tractions from underlying mantle flow), or structural[12,13,26] (for example fossil lithospheric fabric, crustal-scale fault systems and gradients in lithosphere thickness). Proxies for dynamical indicators of deformation are given by the crustal deviatoric stress tensor, and to some degree by seismic anisotropy from SKS splitting measurements, although the source of seismic anisotropy is a matter of much debate[27] and may be complex[28] (that is, vertically layered). We test the hypothesis of dynamical control on T_e anisotropy by comparing ϕ_e to the maximum horizontal

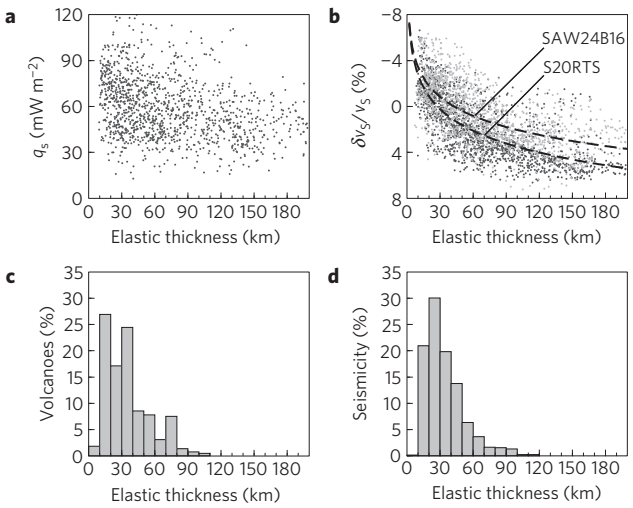

Figure 2 | Correlations between the T_e structure and geophysical data over continents. a, T_e versus surface heat flux obtained from a global compilation averaged on a 2° × 2° grid[21]. Correlation coefficient is −0.32, indicating a poor fit. **b**, T_e versus seismic velocity anomalies at 100 km depth with respect to PREM from two 1° × 1° global models: S20RTS (ref. 22; dark grey dots) and SAW24B16 (ref. 23; lighter grey dots), with correlation coefficients of 0.69 and 0.64, respectively. Dashed lines represent empirical fits using a logarithmic function. Histograms in **c** and **d** show the distribution of seismicity between 1970 and 2009 from the Advanced National Seismic System (ANSS) catalog for volcanoes (**c**) and all events $M > 5$ shallower than 50 km (**d**) within T_e bins of 10 km.

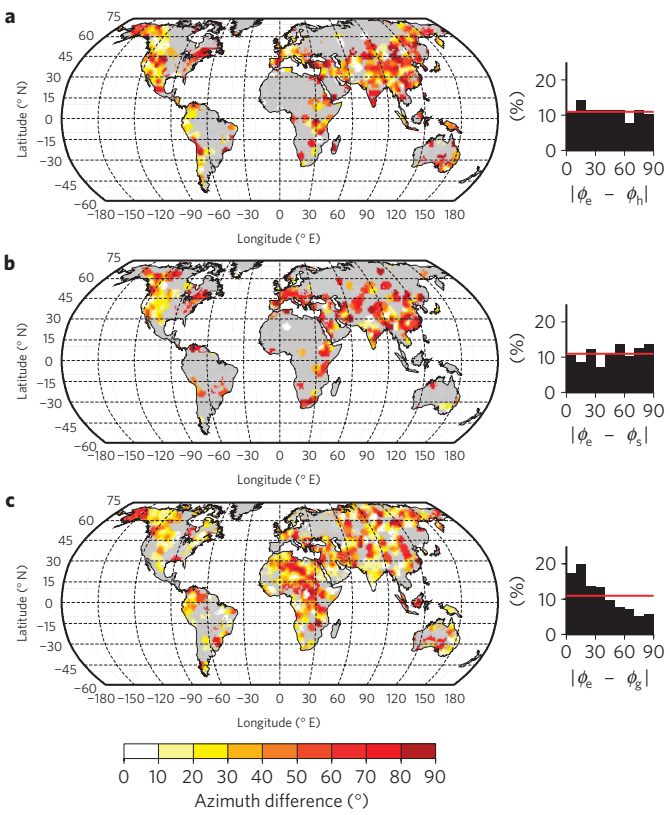

Figure 3 | Angle difference between T_e anisotropy and geophysical indicators of deformation. a, Directions of maximum horizontal compressive stress from the World Stress Map project[29] (**b**) fast directions of shear-wave splitting data[30] and (**c**) directions of maximum T_e gradient. Calculation is carried on a 3° × 3° grid at cells where T_e anisotropy is larger than 0.2, T_e gradient is larger than 0.05, and isotropic T_e estimate is robust. Histograms on the right side of each map show the statistical distribution of alignment. Horizontal red bar corresponds to the expected distribution if there were no correlation between directional indicators. All images are in a Robinson projection with a central meridian of 0° longitude.

principal stress directions (ϕ_h), and directions of fast seismic wave propagation from SKS splitting (ϕ_s). Crustal stress indicators manifest the combined action of plate boundary tractions, internal buoyancy, and crustal strength heterogeneity. Under a compressive stress regime, as observed in most continental regions, ϕ_e and ϕ_h are expected to be aligned[17,25]. The directions of fast seismic wave propagation from SKS splitting measurements are thought to result from the lattice-preferred orientation of olivine crystals and may be taken as proxy for fossil lithosphere fabric, sub-lithospheric mantle flow, or a combination of these[27,28]. In the former case, where ϕ_s is aligned with tectonic trends (perpendicular to the horizontal shortening axis), we expect ϕ_e and ϕ_s to be anti-correlated[12,13,26]. If the cause of ϕ_s variations is sub-lithospheric mantle flow, for example beneath continental interiors away from plate boundaries, we expect some correlation between ϕ_e and ϕ_s if lithosphere–asthenosphere coupling is strong, and random correlation otherwise.

Results of the angular difference between ϕ_e and both ϕ_h and ϕ_s are shown in Fig. 3a,b. We find no systematic correlation between directional indicators except locally in northwestern and eastern North America, and parts of Europe. The results in North America are particularly interesting, as opposite trends are found. At the eastern margin both ϕ_h and ϕ_s align in the direction of absolute plate motion (NE–SW), indicating that seismic anisotropy and crustal stress arise mainly from plate boundary forces and, to some degree, underlying mantle flow. In this region ϕ_e is oriented NW–SE in the direction perpendicular to tectonic trends and faults and is at high angle to both ϕ_h and ϕ_s, indicating a shallow, structural control on mechanical anisotropy. In northwestern North America, all three indicators align in the direction of absolute plate motion and perpendicular to major Cordilleran belts and faults, indicating some combination of dynamical and structural controls on T_e anisotropy. These results may also indicate that stress and seismic anisotropy are controlled by local mantle flow deflection due to gradients in lithosphere thickness[28], consistent with a sharp T_e gradient.

The absence of a global systematic correlation between ϕ_e and both ϕ_h and ϕ_s allows us to infer that (1) dynamical factors are not the dominant controls on mechanical anisotropy of continental lithosphere, and (2) regional correlations between ϕ_e and ϕ_s do not provide insights into global factors controlling T_e anisotropy. To test the second hypothesis, that is, a structural control on T_e anisotropy, we compare ϕ_e to the directional derivative of T_e, ϕ_g, which provides a measure of lateral contrasts in thickness and rheological units, and serves as a proxy for lithospheric fabric. Results are shown in Fig. 3c. We find that ϕ_e is predominantly parallel to ϕ_g and perpendicular to suture zones and most passive continental margins, with particularly good agreement in North and South America, the India–Tibet collision zone, and around the Afar Triple Junction. These results indicate that T_e anisotropy is related to preferential flexural compensation of the lithosphere in the direction perpendicular to major rheological boundaries and support the thesis that mechanical anisotropy is controlled dominantly by pre-existing structure.

These results allow us to clarify the role of rheological heterogeneity and mechanical anisotropy in continental evolution and deformation. That T_e varies according to age since the last thermo-tectonic event and is partitioned between continental cores and margins is consistent with the episodic thermal rejuvenation of continental margins and resetting of lithosphere strength during thermo-tectonic events. These episodes originate from large-scale

vertical convective motion of the mantle during continental assembly and breakup and are accompanied by margin-wide faulting and fault reactivation (either from rifting or thrusting) that further weaken marginal lithosphere and induce significant mechanical anisotropy. A weak and faulted lithosphere may enhance deformation by concentrating strain at pre-existing structures. Over time, these factors isolate continental interiors from deformation due to plate boundary forces during continental assembly and allow only a small fraction of continental lithosphere to get recycled. Only in rare cases do plumes or delamination events de-stabilize cratonic cores. This model is consistent with numerical models of continental evolution that simulate the stability of cratonic crust and longevity of deeper roots as a consequence of higher yield strength with respect to oceanic lithosphere, and the buffering effect of weak mobile belts and margins that absorb stresses during repeated supercontinent cycles[7–9]. This, in turn, implies that the inherited weakness of marginal lithosphere is relatively long-lived, despite its tendency to get recycled into the mantle during orogeny, possibly the result of continuous accretion of terranes and plateaus that further enhances mechanical weakness and anisotropy.

Received 24 May 2010; accepted 11 January 2011; published online 13 February 2011

References

1. Wilson, J. T. Did the Atlantic close and then re-open? *Nature* **211,** 676–681 (1966).
2. Jordan, T. H. Composition and development of the continental tectosphere. *Nature* **274,** 544–548 (1978).
3. Li, Z. X. *et al.* Assembly, configuration, and break-up history of Rodinia: A synthesis. *Precambr. Res.* **160,** 179–210 (2008).
4. Thomas, W. A. Tectonic inheritance at a continental margin. *GSA Today* **16,** 4–11 (2006).
5. Vauchez, A., Tommasi, A. & Barruol, G. Rheological heterogeneity, mechanical anisotropy and deformation of the continental lithosphere. *Tectonophysics* **296,** 61–86 (1998).
6. Gurnis, M. Large-scale mantle convection and the aggregation and dispersal of supercontinents. *Nature* **332,** 695–699 (1988).
7. Gurnis, M., Zhong, S. & Toth, J. in *The History and Dynamics of Global Plate Motions* (eds Richards, M. A., Gordon, R. G. & van der Hilst, R. D.) 73–94 (Am. Geophys. Union, 2000).
8. Lenardic, A., Moresi, L-N. & Mühlhaus, H. Longevity and stability of cratonic lithosphere: Insights from numerical simulations of coupled mantle convection and continental tectonics. *J. Geophys. Res.* **108,** 2303 (2003).
9. Coltice, N. *et al.* Global warming of the mantle as the origin of flood basalts over supercontinents. *Geology* **35,** 391–394 (2007).
10. Watts, A. B. *Isostasy and Flexure of the Lithosphere* (Cambridge Univ. Press, 2001).
11. Burov, E. B. & Diament, M. The effective elastic thickness (T_e) of continental lithosphere: What does it really mean? *J. Geophys. Res.* **100,** 3905–3927 (1995).
12. Kirby, J. F. & Swain, C. J. Mapping the mechanical anisotropy of the lithosphere using a 2D wavelet coherence, and its application to Australia. *Phys. Earth Planet. Int.* **158,** 122–138 (2006).
13. Audet, P. & Mareschal, J-C. Wavelet analysis of the coherence between Bouguer gravity and topography: Application to the elastic thickness anisotropy in the Canadian Shield. *Geophys. J. Int.* **168,** 287–298 (2007).
14. McKenzie, D. Estimating T_e in the presence of internal loads. *J. Geophys. Res.* **108,** 2438 (2003).
15. Kirby, J. F. & Swain, C. J. A reassessment of spectral T_e estimation in continental interiors: The case of North America. *J. Geophys. Res.* **114,** B08401 (2009).
16. Pérez-Gussinyé, M. & Watts, A. B. The long-term strength of Europe and its implications for plate forming processes. *Nature* **436,** 381–384 (2005).
17. Audet, P., Jellinek, A. M. & Uno, H. Mechanical controls on the deformation of continents at convergent margins. *Earth Planet. Sci. Lett.* **264,** 151–166 (2007).
18. Tassara, A., Swain, C., Hackney, R. & Kirby, J. Elastic thickness structure of South America estimated using wavelets and satellite-derived gravity data. *Earth Planet. Sci. Lett.* **253,** 17–36 (2007).
19. Pérez-Gussinyé, *et al.* Effective elastic thickness of Africa and its relationship to other proxies for lithospheric structure and surface tectonics. *Earth Planet. Sci. Lett.* **287,** 152–167 (2009).
20. Artemieva, I. M. Global 1 × 1 thermal model TC1 for the continental lithosphere: Implications for lithosphere secular evolution. *Tectonophysics* **416,** 245–277 (2006).
21. Hyndman, R. D., Currie, C. A. & Mazzotti, S. Subduction zone backarcs, mobile belts, and orogenic heat. *GSA Today* **15,** 4–10 (2005).
22. Ritsema, J., Jan van Heijst, H. & Woodhouse, J. H. Global transition zone tomography. *J. Geophys. Res.* **109,** B02302 (2004).
23. Mégnin, C. & Romanowicz, B. The shear velocity structure of the mantle from the inversion of body, surface and higher modes waveforms. *Geophys. J. Int.* **143,** 709–728 (2000).
24. Hyndman, R. D., Currie, C. A., Mazzotti, S. & Frederiksen, A. Temperature control of continental lithosphere elastic thickness, *Te* vs *Vs*. *Earth Planet. Sci. Lett.* **277,** 539–548 (2009).
25. Lowry, A. R. & Smith, R. B. Strength and rheology of the western US Cordillera. *J. Geophys. Res.* **100,** 17947–17963 (1995).
26. Simons, F. J. & van der Hilst, R. D. Seismic and mechanical anisotropy and the past and present deformation of the Australian lithosphere. *Earth Planet. Sci. Lett.* **211,** 271–286 (2003).
27. Fouch, M. J. & Rondenay, S. Seismic anisotropy beneath stable continental interiors. *Phys. Earth Planet. Int.* **158,** 292–320 (2006).
28. Yuan, H. & Romanowicz, B. Lithospheric layering in the North American craton. *Nature* **466,** 1063–1068 (2010).
29. Heidbach, O. *et al.* The World Stress Map database release 2008, http://dc-app3-14.gfz-potsdam.de/index.html (2008).
30. Wüstefeld, A., Bokelmann, G., Barruol, G. & Montagner, J-P. Identifying global seismic anisotropy patterns by correlating shear-wave splitting and surface-wave data. *Phys. Earth Planet. Int.* **176,** 198–212 (2009).

Acknowledgements

This work is supported by the Miller Institute for Basic Research in Science (UC Berkeley).

Author contributions

P.A. performed data processing and inversion. P.A. and R.B. wrote the paper.

Additional information

The authors declare no competing financial interests. Supplementary information accompanies this paper on www.nature.com/naturegeoscience. Reprints and permissions information is available online at http://npg.nature.com/reprintsandpermissions. Correspondence and requests for materials should be addressed to P.A.

nature geoscience
SUPPLEMENTARY INFORMATION
DOI: 10.1038/NGEO1080

Dominant role of tectonic inheritance in supercontinent cycles

Data and method

Estimates of the effective elastic thickness, T_e, are obtained by minimizing the least-square misfit between the observed coherence between Bouguer gravity and topography with the coherence predicted by the flexure of a thin (isotropic or orthotropic) elastic plate bending under surface and internal loading. We use the $1' \times 1'$ SRTM bathymetry/topography and model of Smith & Sandwell[1,2] and the gravity model EGM2008[3,4]. We extract data for each continent on Transverse Mercator grids to preserve angles. Free-air gravity anomaly is converted to Bouguer anomaly using the FA2BOUG[5] software using grid steps for the distant and intermediate zones of 10 and 5 km. The final Bouguer grid is calculated on a 20×20 km^2 grid. The continents of Greenland and Antarctica were excluded from the analysis due to limited coverage near the poles (SRTM data is limited to $\pm 81°$), and to avoid complications due to ice loading. After inversion, all T_e estimates are back-projected on a $10' \times 10'$ grid, whereas T_e anisotropy is calculated on a $3° \times 3°$ grid. The coherence is calculated using a wavelet transform method[6,7]. The Morlet wavelet is chosen to produce directional estimates of wavelet auto- and cross-spectra, and thus to calculate two-dimensional coherence. Because wavelets are designed to afford optimal resolution in both spectral and spatial domains (with some trade-off due to uncertainty principle), T_e can be calculated at each grid point without the limitations caused by calculating T_e within finite windows, thus resolving longer wavelengths and allowing the estimation of large T_e values. By doing so we implicitly assume that spatially adjacent spectra (or coherence) are statistically independent in

DOI: 10.1038/NGEO1080

order to evaluate T_e; however the error introduced is small compared to the large spatial variability observed.

In the inversion, the predicted coherence is calculated by deconvolving the topography and Bouguer gravity into surface and internal components of the statistically-uncorrelated initial loading structure[8]. Water load is converted to equivalent rock load by scaling the bathymetry using $h(\mathbf{r}) \rightarrow \left(\frac{\rho_c - \rho_w}{\rho_c}\right) h(\mathbf{r})$, where $h(\mathbf{r})$ is bathymetry ($h(\mathbf{r}) < 0$), and ρ_c and ρ_w are density of the crust and water, respectively. The load deconvolution step requires information on the crustal structure that we extract from the CRUST2.0 model[9]. Several studies have shown that errors in crustal structure have little effects on the recovered T_e[10,11]. We take the subsurface load to be the density contrast between the crustal average and underlying mantle, and place it at lower crustal depth. The flexural rigidity is converted to T_e using a Poisson's ratio of 0.25 and Young modulus of 100 GPa from the relation

$$D = \frac{ET_e^3}{12(1-\nu^2)}. \tag{1}$$

The un-filtered T_e map is shown in Figure S1a. We calculate confidence intervals on both T_e and ϕ_e from the chi-square (χ^2) error distribution, using variance of individual measurements calculated from the jackknife method. For isotropic T_e the uncertainty corresponds to the 95% (2-σ) confidence intervals. Results are shown in Figure S1b. Large errors are associated with large T_e values. The median T_e error is 5 km over continents. For the anisotropic inversion we evaluate the 68% (1-σ) confidence intervals, and the results are shown in Figure S1c.

The Bouguer coherence method has been shown to provide overestimates of T_e in regions

where gravitational "noise", defined as topographically unexpressed internal gravity anomalies, is present[12,13]. Using numerical simulations, Crosby[14] has shown that such large and widespread "noise" (i.e., having a white spectrum) is indeed likely to bias the coherence. Kirby and Swain[11] confirmed these results using numerical simulations, but further showed that both free-air admittance and Bouguer coherence methods were affected in the case of widespread "noise". Furthermore, they propose a method to detect the "noise" based on the imaginary component of the free-air coherency spectrum and show that T_e estimates will be biased only if the imaginary free-air coherency peaks close to the transition wavelength (from low to high admittance and/or coherence). Using this diagnostic tool, they calculate T_e within continental North America and mask out the regions showing large "noise" effect. Here we calculate T_e using the Bouguer coherence method and mask out regions where gravitational "noise" affects the estimates as suggested by Kirby and Swain[11]. A T_e estimate is biased if the maximum normalized imaginary component of free-air coherency, over wavenumbers immediately below the Bouguer transition wavelength, is larger than 0.4. We check the robustness of the inversion by calculating the wavelet Bouguer admittance and compare it with the admittance predicted from the best-fit solution of the initial loading structure. The same procedure is performed for the 2-D estimates, and we characterize "noise" as a function of azimuth. Figures S2 to S7 show example results for both biased (panels **b**) and robust estimates (panels **c-e**). We also report estimates of subsurface-to-surface loading ratio F at all locations. We emphasize that while large gravitational "noise" indicates a failure of the plate loading model (and T_e estimation from gravity-topography spectra), it does not imply that the lithosphere is weak. Indeed, we show that regions affected by the "noise" are surrounded by large T_e areas, suggesting

DOI: 10.1038/NGEO1080

that those regions may also have large T_e values. We note that directional bias is weakly correlated with anisotropic T_e directions and coincides with isotropic bias. This implies that isotropic "noise" arises from the azimuthal averaging of large directional "noise", which is more likely to be related to the anisotropy in initial loading structure than to directionally-varying lithospheric strength. The origin of such "noise" has been attributed to the erosion of surface topography associated with large initial loads, or to basin infilling following lower crustal modifications [11,13]. If those loads are anisotropic, the resulting bias will show a strong directional response. Finally, we apply a Gaussian filter of width 900 km to all T_e results (including biased T_e estimtes) to obtain a smooth T_e gradient map. Directional derivative is calculated on a $3^\circ \times 3^\circ$ grid from the filtered T_e map.

Geophysical correlations

Figures S8 and S9 show the various data sets used in the comparison with T_e. Surface heat flux (q_s) data are taken from the compilation of the International Heat Flow Commission (IHFC) (Figure S8). Seismic veolcities are taken at a depth of 100 km using two published models: S20RTS[15] and SAW24B16[16] (Figure S9). The correlation coefficients (Figure 2a,b) are calculated by linearizing the relationship between T_e and heat flow and seismic velocities using a simple polynomial fit. In Figure S10 we show the comparison between directional indicators. Results are plotted where magnitude of T_e anisotropy is larger than 0.2, and magnitude of T_e gradient is larger than 0.5 (Figure S10c).

In this paper we show that T_e gradients (i.e., spatial variability), and T_e anisotropy (i.e., directional variability) are independent and complementary measures of deformation on a global scale; however, we note that more work is required to explore this relationship in detail (e.g., parameterized numerical modelling of plate deformation; detailed regional analysis, etc.).

1. Smith, W. H. F. & Sandwell, D. T. Global sea floor topography from satellite altimetry and ship depth soundings. *Science* **277**, 1956–1962 (1997).

2. `http://topex.ucsd.edu/`.

3. Pavlis, N. K., Holmes, S. A., Kenyon, S. C. & Factor, J. K. An earth gravitational model to degree 2160: EGM2008. In *Abstracts with Programs, European Geosciences Union, 2008 General Assembly* (European Geosciences Union, 2008).

4. `http://earth-info.nga.mil/GandG/wgs84/gravitymod/egm2008/`.

5. Fullea, J., Fernández, M. & Zeyen, H. FA2BOUG-A FORTRAN 90 code to compute Bouguer gravity anomalies from gridded free-air anomalies: Application to the Atlantic-Mediterranean transition zone. *Comput. Geosci.* **34**, 1665–1681 (2008).

6. Audet, P. & Mareschal, J.-C. Wavelet analysis of the coherence between Bouguer gravity and topography: Application to the elastic thickness anisotropy in the Canadian Shield. *Geophys. J. Int.* **168**, 287–298 (2007).

DOI: 10.1038/NGEO1080

7. Kirby, J. F. & Swain, C. J. Mapping the mechanical anisotropy of the lithosphere using a 2-D wavelet coherence, and its application to Australia. *Phys. Earth Planet. Int.* **158**, 122–138 (2006).

8. Pérez-Gussinyé, M., Lowry, A., Watts, A. B. & Velicogna, I. On the recovery of effective elastic thickness using spectral methods: Examples from synthetic data and from the Fennoscandian Shield. *J. Geophys. Res.* **109**, B10409, doi:10.1029/2003JB002788 (2004).

9. Bassin, C., Laske, G. & Masters, G. The current limits of resolution for surface wave tomography in North America. *EOS Trans AGU* **81**, F897 (2000).

10. Pérez-Gussinyé, M. *et al.* Effective elastic thickness of Africa and its relationship to other proxies for lithospheric strucgture and surface tectonics. *Earth Planet. Sci. Lett.* **287**, 152–167 (2009).

11. Kirby, J. F. & Swain, C. J. A reassessment of spectral T_e estimation in continental interiors: The case of North America. *J. Geophys. Res.* **114**, B08401, doi:10.1029/2009JB006356 (2009).

12. McKenzie, D. P. & Fairhead, J. D. Estimates of the effective elastic thickness of the continental lithosphere from Bouguer and free air gravity anomalies. *J. Geophys. Res.* **102**, 27523–27552 (1997).

13. McKenzie, D. Estimating T_e in the presence of internal loads. *J. Geophys. Res.* **108**, 2348, doi:10.1029/2002JB001766 (2003).

14. Crosby, A. G. An assessment of the accuracy of admittance and coherence estimates using synthetic data. *Geophys. J. Int.* **171**, 25–54, doi:10.1111/j.1365–246X.2007.03520 (2007).

15. Ritsema, J., Jan van Heist, J. & Woodhouse, J. H. Global transition zone tomography. *J. Geophys. Res.* **109**, B02302, doi:10.1029/2003JB002610 (2004).

16. Mégnin, C. & Romanowicz, B. The shear velocity structure of the mantle from the inversion of body, surface and higher modes waveforms. *Geophys. J. Int.* **143**, 709–728 (2000).

DOI: 10.1038/NGEO1080

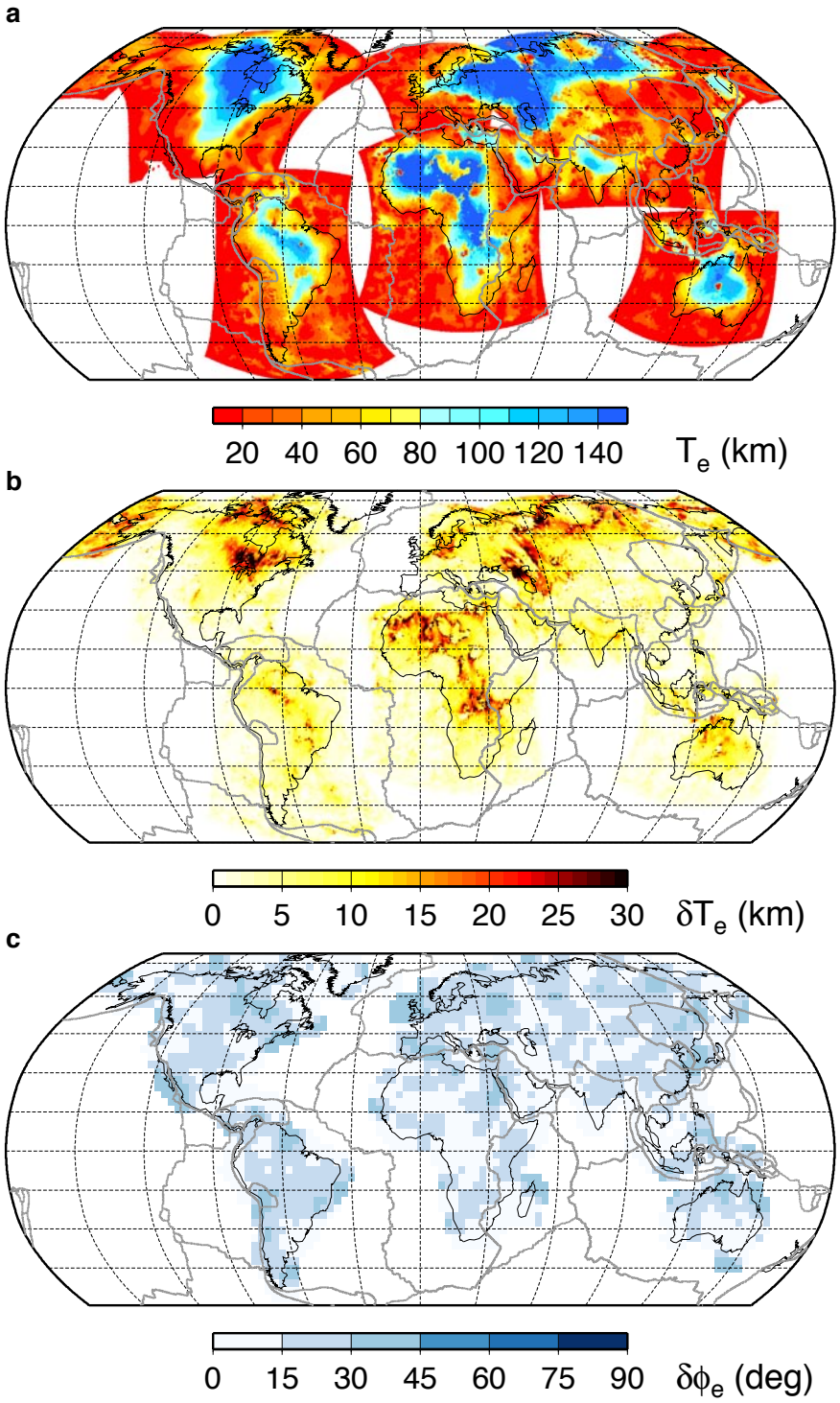

Figure S1. **a**, Unfiltered global T_e map; **b**, T_e error (δT_e); and **c**, error in azimuth of weak direction ($\delta\phi_e$). The shape of the Transverse Mercator grids used for each continent is clearly visible in **a**,. δT_e is positively correlated with T_e, however most continental areas show $\delta T_e < 20$ km. Median errors for T_e and ϕ_e are 5 km and 10° over continents, respectively.

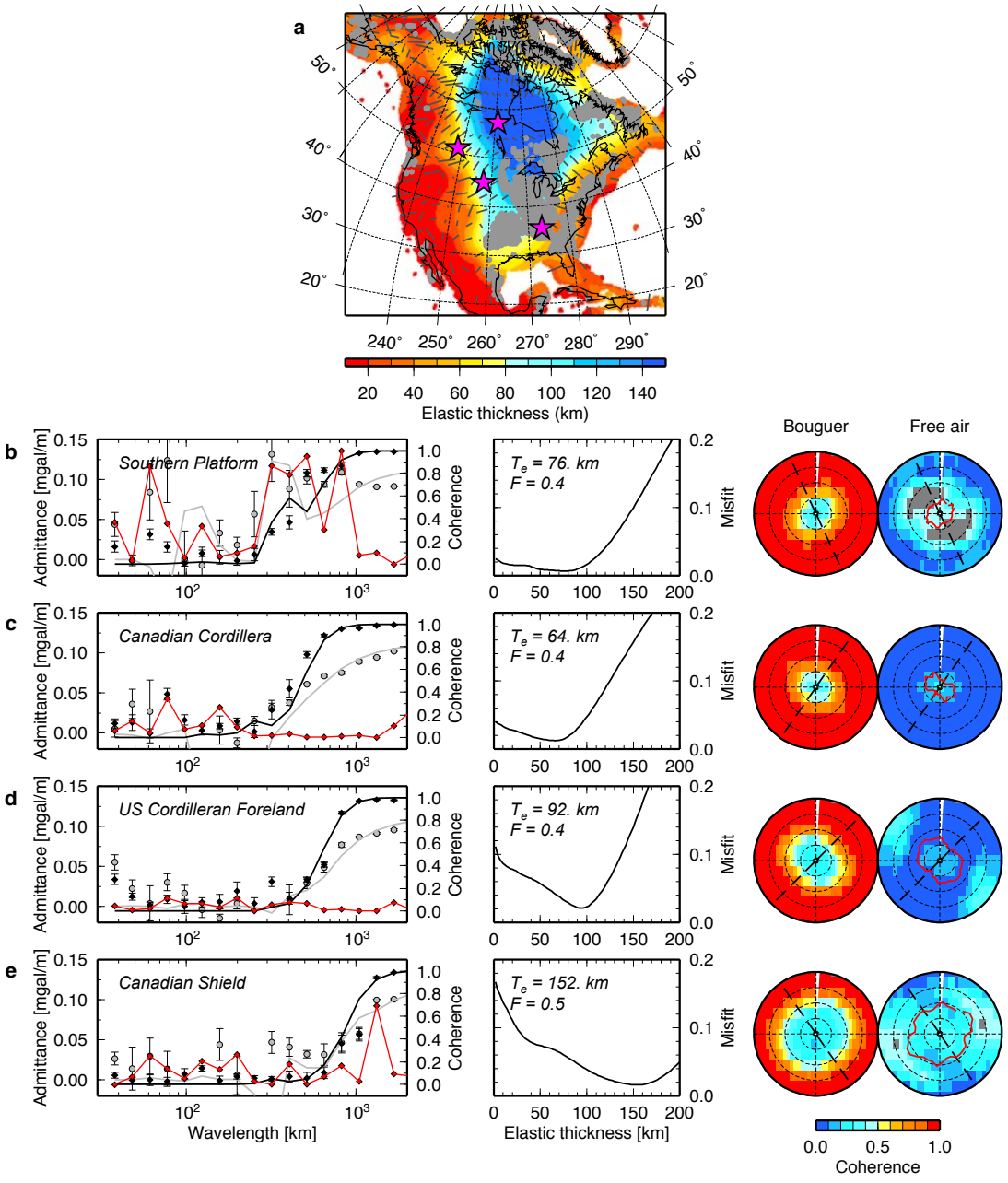

Figure S2. **a**, Filtered T_e and T_e anisotropy over North America. Shaded areas show regions where T_e estimation is biased by "noise". Stars indicate the locations where 1D and 2D coherence and admittance are plotted in **b-e**. Left panels: observed (circles) and predicted (lines) 1D Bouguer coherence (black) and negative admittance (grey). Red circles and lines are observed normalized imaginary free-air coherency. Central panels: misfit curves used to estimate T_e using Bouguer coherence and load ratio F. Right panels: observed 2D Bouguer coherence and imaginary free-air coherency shown as stereographic polar plots; wavelengths increase radially. Black dashed lines indicate azimuth of the weak direction. Red contours show Bouguer coherence transition wavelength. Grey shades represent high noise levels. **b**, example of T_e estimate biased by "noise".

DOI: 10.1038/NGEO1080

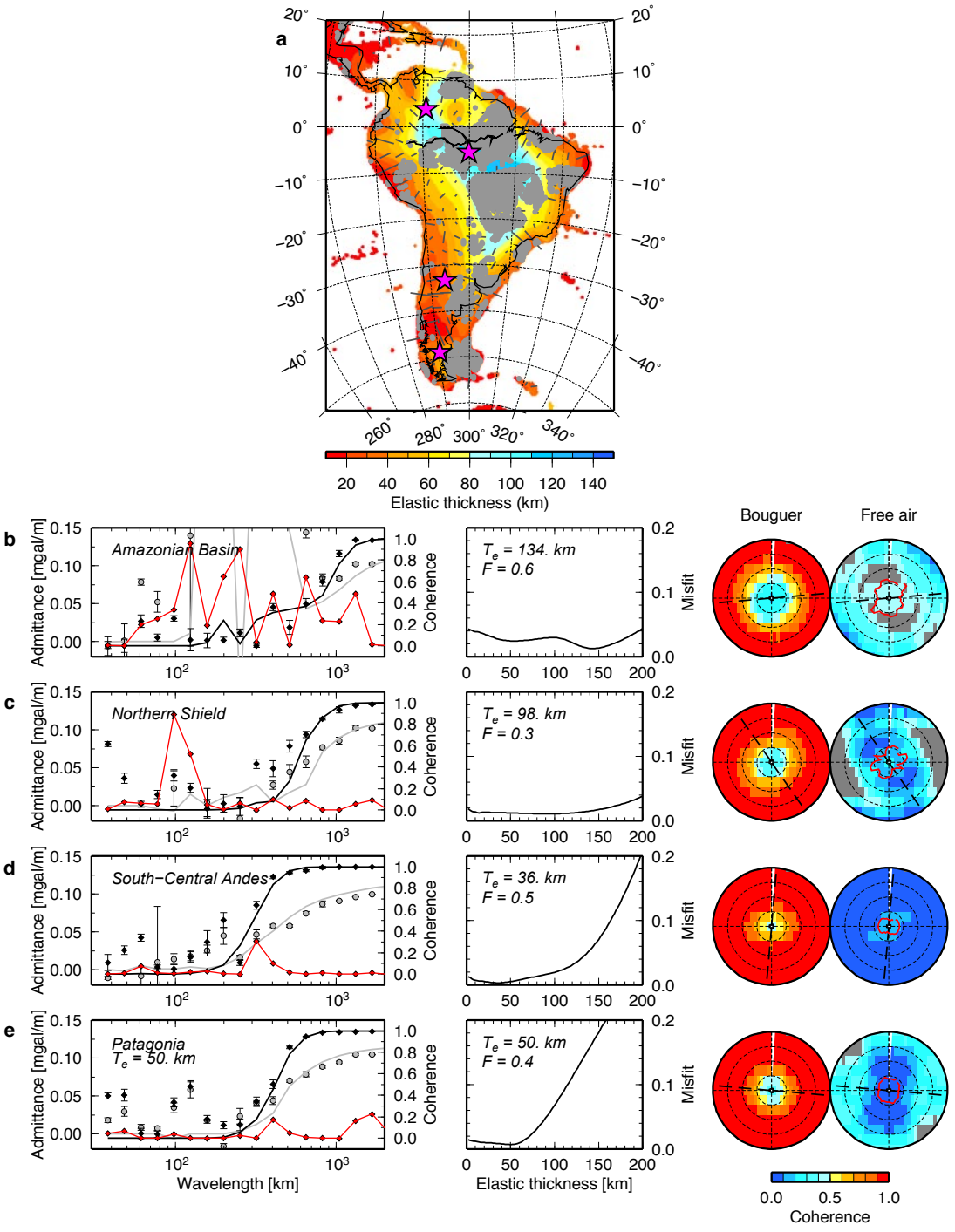

Figure S3. Same as Figure S2 for South America.

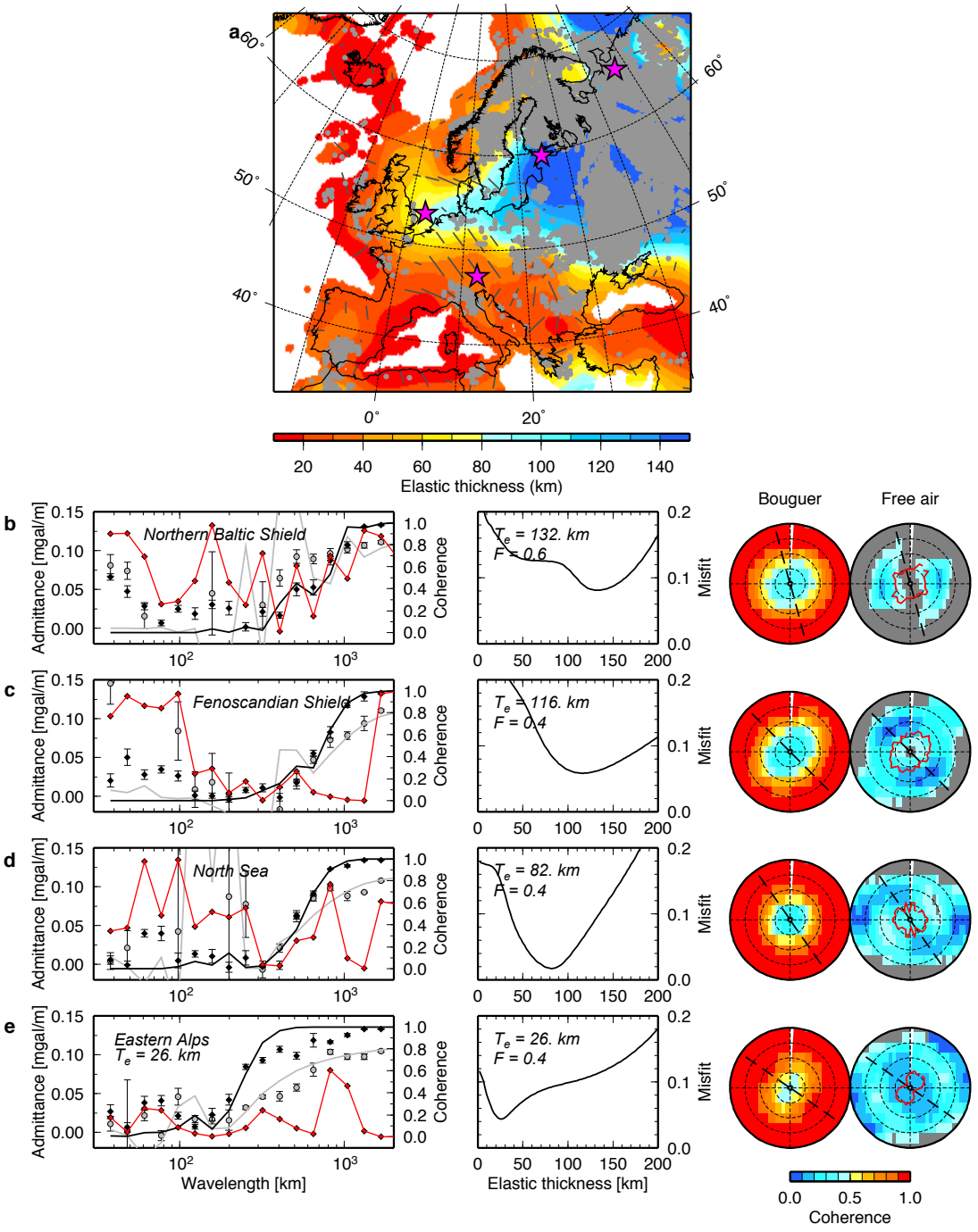

Figure S4. Same as Figure S2 for Europe.

DOI: 10.1038/NGEO1080

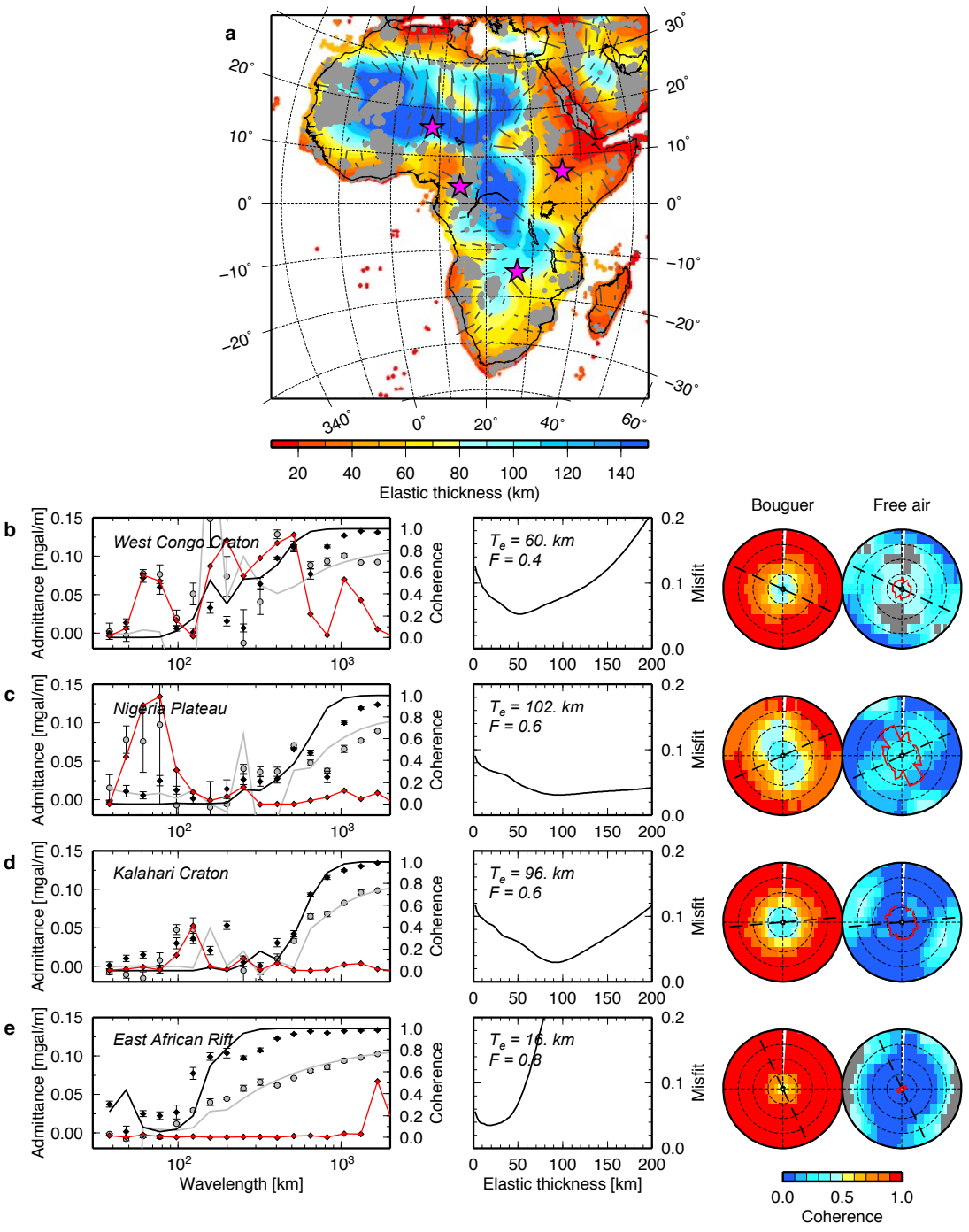

Figure S5. Same as Figure S2 for Africa.

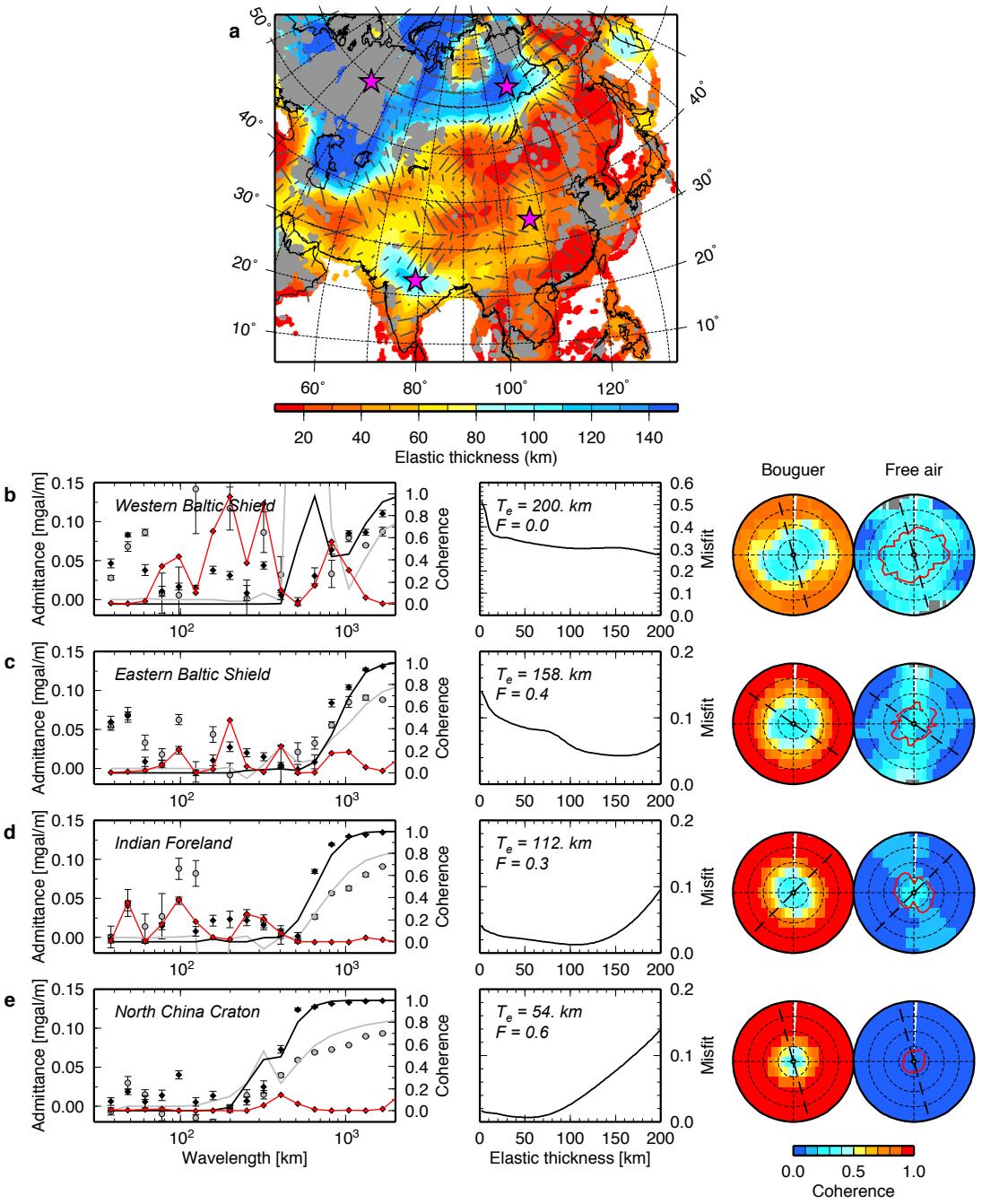

Figure S6. Same as Figure S2 for Asia.

DOI: 10.1038/NGEO1080

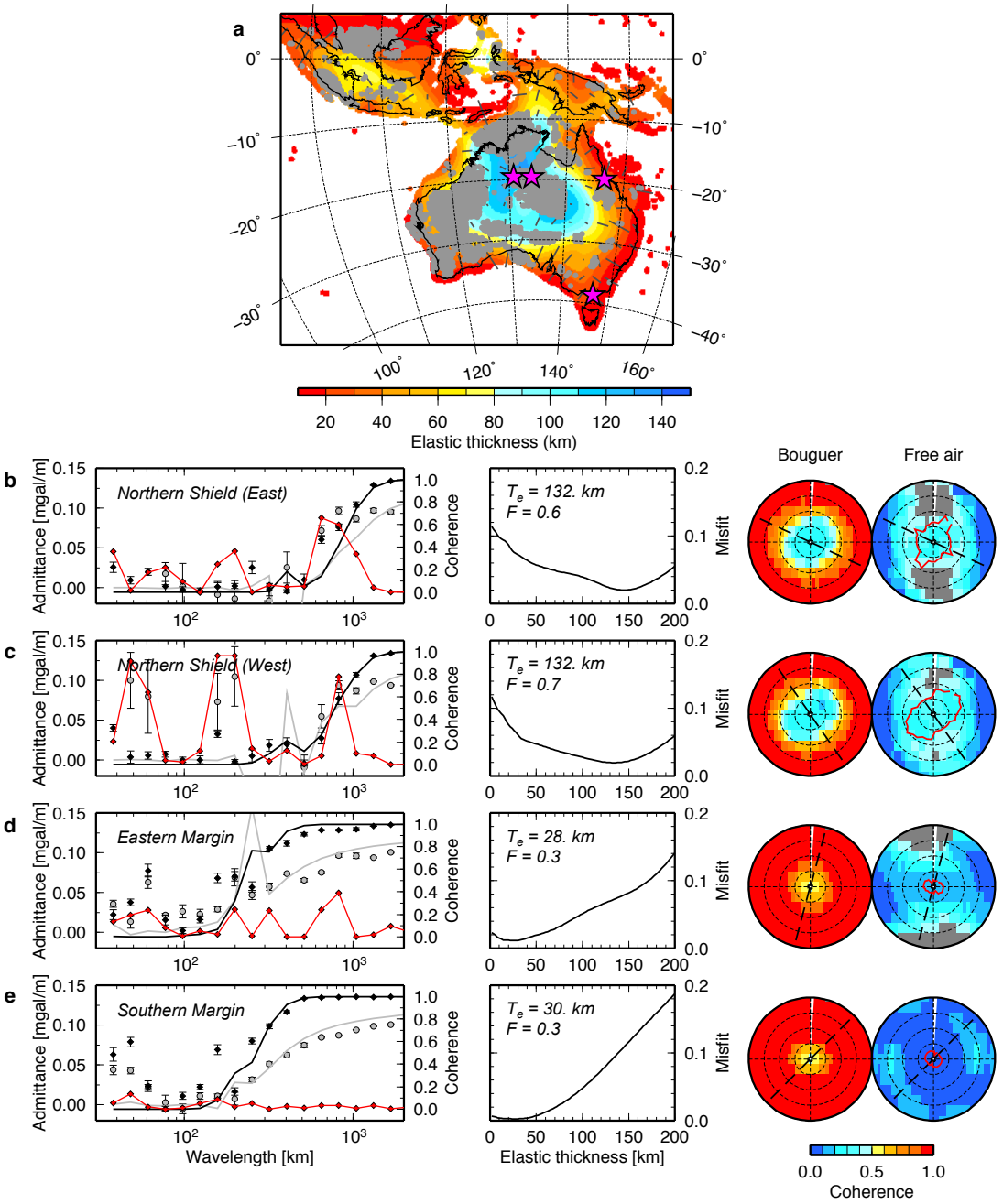

Figure S7. Same as Figure for Australia.

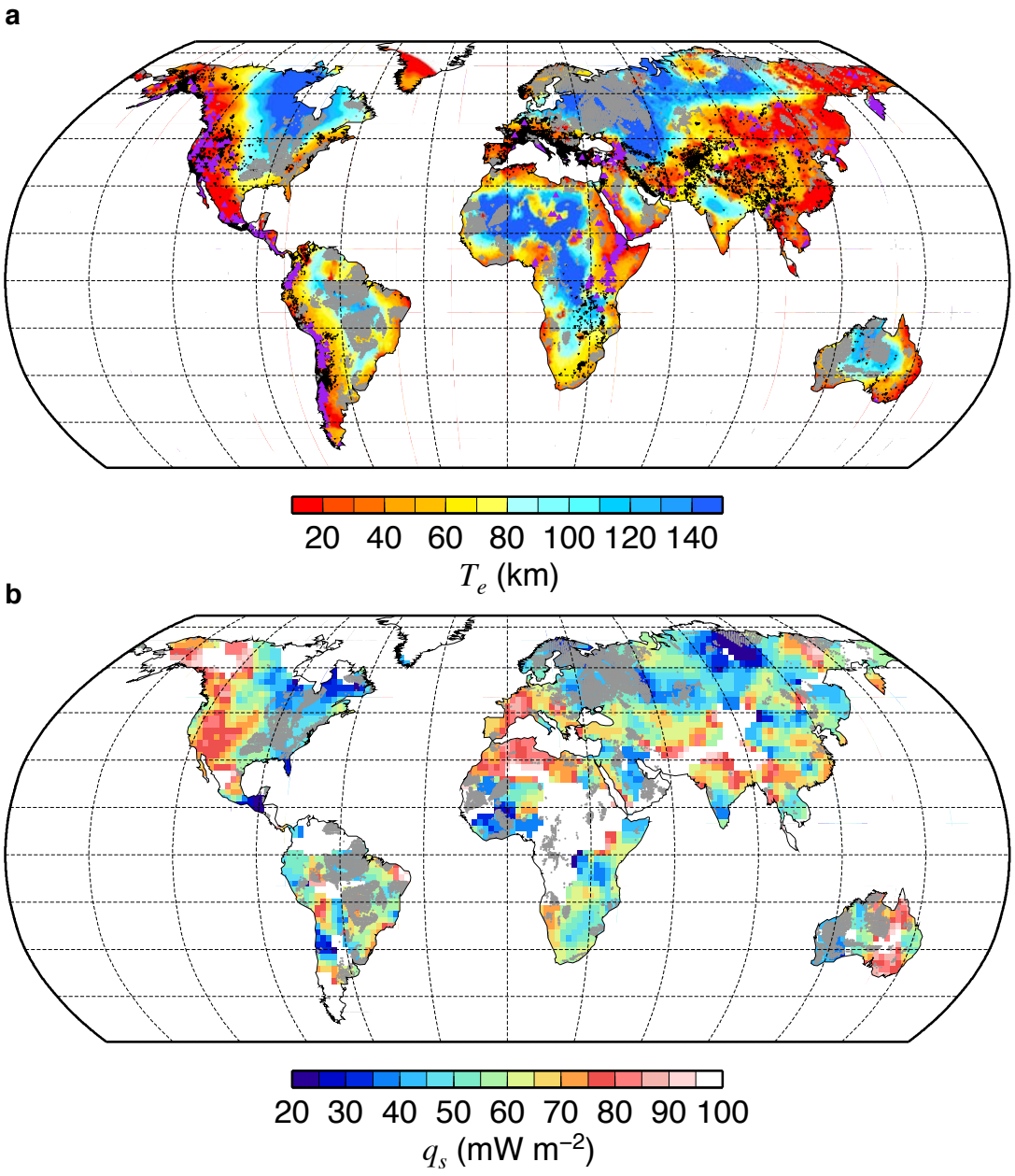

Figure S8. **a**, Unfiltered global T_e map with earthquakes shallower than 50 km (black dots) and volcanic centers (purple triangles) superposed; **b**, surface heat flux map on a $2^\circ \times 2^\circ$ grid. Shaded areas show regions where T_e estimation is biased by "noise".

DOI: 10.1038/NGEO1080

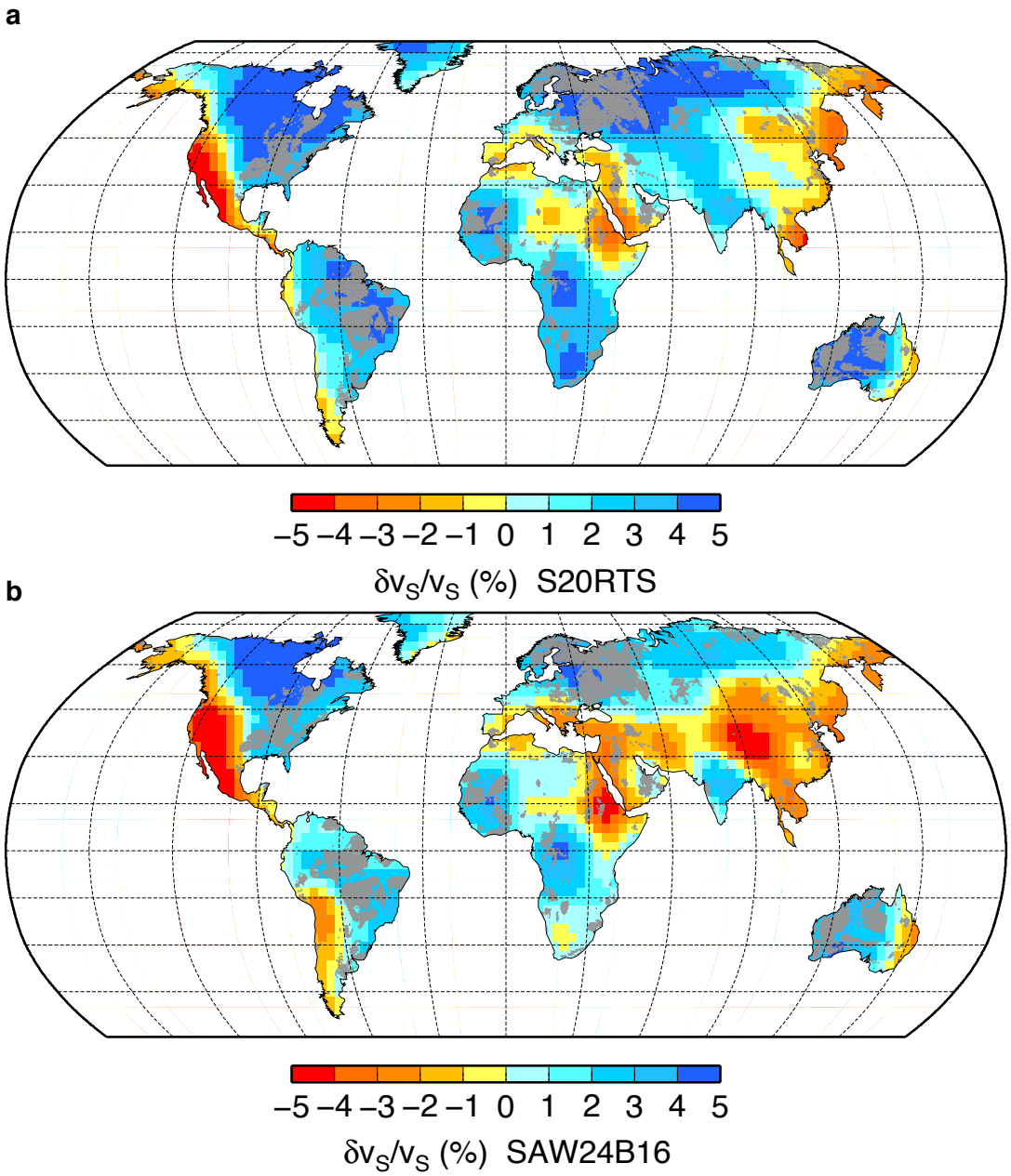

Figure S9. **a,b**, seismic velocity anomalies at 100 km depth on a $3^\circ \times 3^\circ$ grid from the S20RTS (**a**) and SAW24B16 (**b**) models. Shaded areas show regions where T_e estimation is biased by "noise".

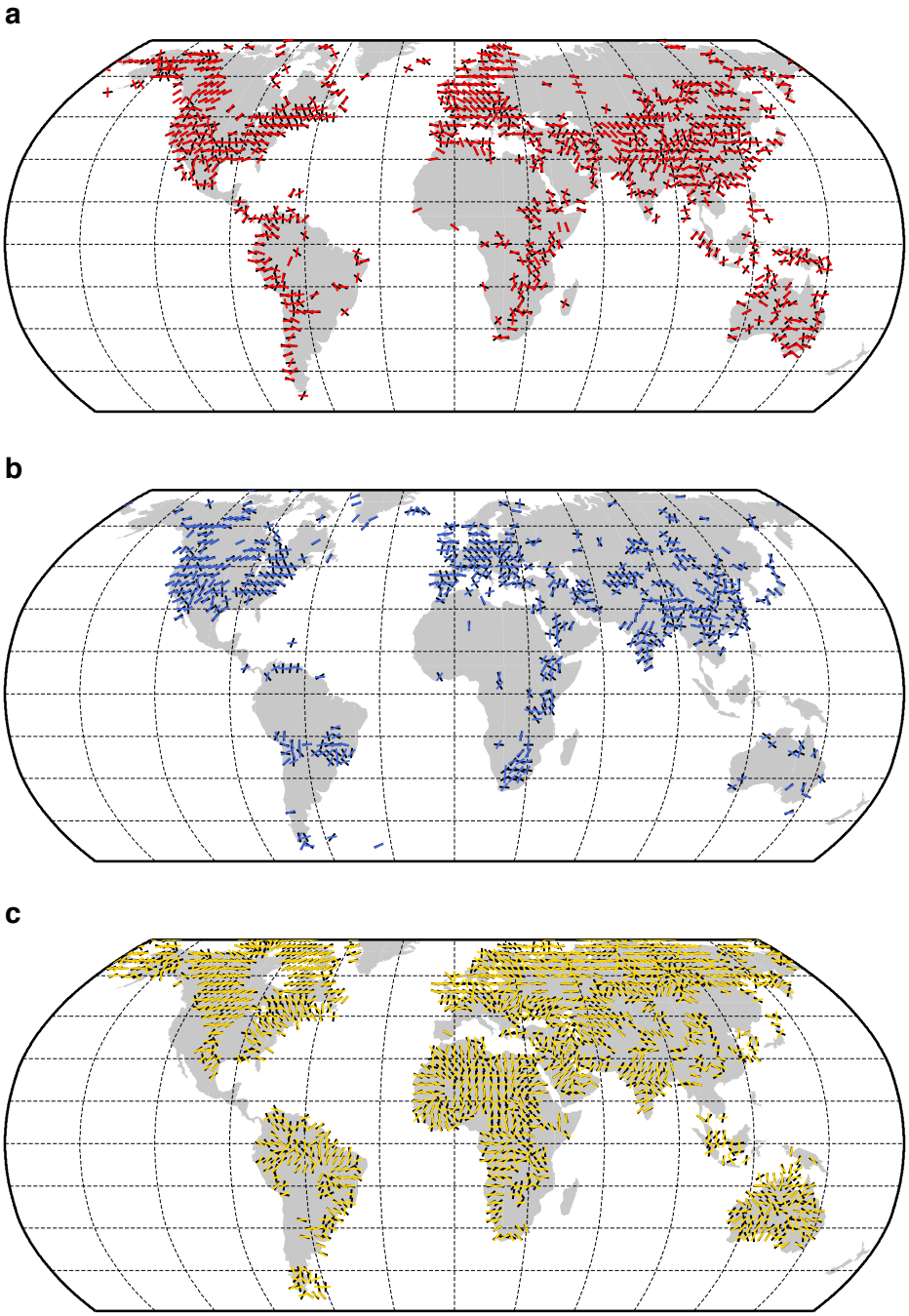

Figure S10. Comparison between weak directions of T_e anisotropy (black bars) and **a**, maximum horizontal compressive stress directions (red); **b**, directions of fast seismic wave propagation of SKS phases (blue); and **c**, directional derivative of T_e (gold).